Post-print version:

CONTROL OF A LITHIUM BATTERY STORAGE SYSTEM FOR MICROGRID APPLICATIONS

J. Pegueroles-Queralt and F.D. Bianchi and O. Gomis-Bellmunt

BibTex:

```
@Article{Pegueroles-Queralt2014,
    Title   = {Control of a lithium battery storage system for microgrid
        applications},
    Author  = {Jordi Pegueroles-Queralt and Fernando D. Bianchi and Oriol
        Gomis-Bellmunt},
    Journal = {Journal of Power Sources},
    Year    = {2014},
    Number  = {1},
    Pages   = {531-540},
    Volume  = {272},
    Doi     = {10.1016/j.jpowsour.2014.08.087}
}
```

Control of a lithium-ion battery storage system for microgrid applications[☆]

Jordi Pegueroles-Queralt[1,*], Fernando D. Bianchi[1], Oriol Gomis-Bellmunt[1,2]

Abstract

The operation of future microgrids will require the use of energy storage systems employing power electronics voltage converters with advanced power management capacities. This paper presents the control scheme for a medium power lithium-ion battery power converter intended for microgrid applications. A combination of a sliding mode control along with a linear regulator scheme is proposed to control a bidirectional DC/AC converter, capable of automatically cover all possible operation states. The switching devices are commanded by a single sliding mode control law, dynamically shaped by a linear voltage regulator in accordance with the battery management system. The sliding mode controller facilitates the implementation and design of the control law and simplifies the stability analysis over the entire operating range. The effectiveness of the proposed control strategy is illustrated by experimental results.

[*]Corresponding author. Email: jpegueroles at irec.cat
[1]Authors are with the Catalonia Institute for Energy Research, IREC, Jardins de les Dones de Negre 1, 08930 Sant Adrià de Besòs (Barcelona), Spain
[2]Is also with CITCEA, ETSEIB, Av. Diagonal, 647. Planta 2, 08028 Barcelona

1. Introduction

Microgrids have become the paradigm for the introduction of distributed renewable power sources in power systems Lasseter (2007); Valverde et al. (2013). Microgrids combine a number of different power sources and loads together with a coordinated management system providing the capability of maintaining the operation even with the microgrid disconnected from the utility. To provide high power quality, the fluctuating renewable power sources must be smoothed with storage systems Diaz-Gonzalez et al. (2014); Guerrero et al. (2013). Medium power lithium-ion batteries are suitable storage systems for providing islanding capabilities Qian et al. (2011); Satpathy et al. (2014).

The main functional requirement of energy storage systems (ESS), when used in microgrids, is to optimize the power flow, usually in terms of energy costs. Depending on the microgrid state, grid connected or islanded, the power flow is determined on a different control agent. On the one hand, when working grid connected, a central energy management system sets the power set-point to every P-Q control of each ESS in the microgrid. On the other hand, when islanded, each ESS determines locally its own power set-point by regulating the voltage and frequency. The common control scheme used to implement the local control is the droop control, see *e.g.* Barklund et al. (2008); Delghavi and Yazdani (2012). Medium power lithium-ion batteries are equipped with a battery management system (BMS) monitoring critical

2

parameters of the battery, providing technical limits for the battery current and voltage.

To implement the functional and technical requirements, ESS can be interfaced with a two stage bidirectional power converter to the microgrid Kuperman et al. (2013). Two stage power converters are necessary in DC-AC systems with different voltage levels at the converter input and output. The first stage is a DC-DC voltage regulator, namely the energy storage side converter (ESSC), which controls the DC-link voltage through the regulation of the battery current. The DC-link voltage must be kept in a narrow band to provide an almost constant DC voltage source to the grid side converter (GSC) Marra et al. (2013), the second stage of the power electronic DC-AC inverter. The ESSC must also guarantee that the BMS limits are never exceeded, performing a tight regulation of the charging/discharging current over all the operating conditions required by lithium-ion batteries Buller et al. (2005).

Different topologies of DC-DC converters are available in the literature, ranging from simple buck or boost converters Sable et al. (1992); Caricchi et al. (1998) to more complex structures based on dual active bridge (DAB) Oggier et al. (2011). The application of power converters to energy storage systems has also been addressed. In Kuperman et al. (2013), a battery charge station for electrical vehicle is presented but the charge algorithm is limited to a constant current and constant voltage operation. Other authors (see *e.g.* Falahi et al. (2013); Levron et al. (2013)) study the management of storage systems, but do not deepen in the low level control of such systems. In Inthamoussou et al. (2013), a power control for supercapacitor storage

systems based on sliding mode (SM) control is proposed. A comprehensive study of SM controlled DC-DC converters has been reported in Barrado et al. (2012), analyzing the performance and stability of the battery side current regulation. However, to the authors' best knowledge, the low level control of power converters for battery storage systems taking into account the requirements of microgrids has not been treated in the literature.

The main contribution of this work is to propose a new control strategy for the regulation of the DC-link voltage using the battery side converter, taking into account the requirements and limitations of medium power lithium-ion batteries when used in microgrids applications. Similar control scheme can be found in Barrado et al. (2012); Inthamoussou et al. (2013), although these schemes does not consider the voltage control of the DC-link. The proposed strategy covers all ESS operating conditions: DC-link pre-charge, DC-link regulation and battery charge/discharge finalization. The strategy is implemented combining SM theory and linear regulators. SM is a nonlinear technique based on variable structures systems resulting especially suitable for switched systems such as power converters Utkin et al. (2009); Park and Gajic (2014). SM permits the combination of designs with different objectives and also provide a quite simple implementation Tan et al. (2008). This combination of different techniques offers the robustness of SM control, a smooth transition between operating conditions and a simple implementation and tuning. The proposed controller changes automatically the set-points according to the BMS, permitting the operation of the power converter in the different operating modes. The proposed ideas are experimentally implemented in a 4 kVA power converter interfacing a 240 V, 20 kW lithium-ion

4

battery with a 400 V AC grid.

2. Energy Storage Systems Based on Lithium-ion Batteries for microgrids

Microgrids are small power systems capable of autonomous operation, *i.e.*, they can work isolated from the distribution grid. To meet the electrical power demand, renewable power sources need to be supported by ESS, acting as voltage sources to maintain the island voltage magnitude and frequency Peças Lopes et al. (2006). ESS are usually composed by an energy storage device and a power electronic converter for the management and electrical interconnection of the DC voltage storage device and the AC grid. The adopted topology for the control of the power flow between the battery and the microgrid is illustrated in Fig. 1. The DC-AC converter is composed of the DC-DC ESSC with a controller K_{ESSC} regulating the DC-link voltage and the GSC with controller K_{GSC} regulating the active and reactive power.

2.1. Ancillary services of batteries in microgrids

When batteries are used in islanded microgrids, there are some functional requirements that must be met. This functions are implemented in the power electronic interface, by means of the control algorithms implemented in K_{ESSC} and K_{GSC}, and also in the microgrid central controller. The following services should be implemented.

1. Regulation of the AC active and reactive power. The power set-points can be given by either a high level microgrid energy management system or a local droop control. The droop control is commonly used as the

power sharing mechanism for isolated micorgrids, see *e.g.* Peças Lopes et al. (2006). In either case, the control producing power references P^* and Q^* must take into account the battery state. For instance, active power set-point can not request charging the battery if this is full.

2. Black-start capability. The DC-link voltage must be pre-charged from the battery, with the DC-DC converter acting as a boost.

3. Safety protections in case of over/under discharge. The ESSC must limit the charging or discharging current in accordance with the BMS signals.

In the following sections, these functions will be analyzed in detail, altogether with the control strategies and implementation details.

2.2. Grid side converter

The GSC is a three phase, two-level voltage source converter. The model of the GSC with the inductive output filter L_f can be expressed in the DQ frame as

$$
\frac{d}{dt} \begin{bmatrix} i_d \\ i_q \end{bmatrix} = \begin{bmatrix} \frac{-Rf}{Lf} & \omega_n \\ -\omega_n & \frac{-Rf}{Lf} \end{bmatrix} \begin{bmatrix} i_d \\ i_q \end{bmatrix} + \frac{1}{Lf} \begin{bmatrix} v_{d_o} - v_d \\ v_{q_o} - v_q \end{bmatrix}, \tag{1}
$$

where $i_{d,q}$ are the AC currents in DQ frame, R_f and L_f are the resistance and inductance of the output filter respectively, v_{d,q_o} are the output voltage of the converter and $v_{d,q}$ are grid voltages, both in DQ frame, and ω_n is the AC voltage frequency.

For the sake of simplicity and to focus on the control strategy of the ESSC, we will use K_{GSC} as an AC active and reactive power controller, using a single current control loop in the DQ axis. This control scheme is much

simpler than the typical droop control scheme used in islanded microgrids. However, this power loop and the droop control behaves identically from the K_{ESSC} control design point of view, acting as a DC current source for the DC-link.

2.3. Energy storage side converter

The topology selected for this application is a buck-boost converter based on a switched branch with an L-filter inductance, shown in Fig. 2. In the literature it can also be found implementations using an output LCL-filter Barrado et al. (2012). In this paper, an L-filter has been chosen as it is the most common filter type for low voltage DC-DC converters adopted by industry Erb et al. (2010).

In medium power battery systems, the BMS provides the charging sequence, indicating the instantaneous maximum dynamic charge and discharge current (MCC, MDC) and the battery maximum charge and discharge voltages (MCV, MDV). To preserve the battery life, the current must remain below MCC and over MDC, and the battery voltage must lie between MCV and MDV, as shown in the charge profile in Fig. 3.

To derive an instantaneous model of the DC-DC power converter, it can be assumed that the voltage is always higher on the DC-link (V_{DC}) than on the battery side (V_B), although energy can flow in both directions. Switches S_{w1} and S_{w2} are operated in a complementary manner, avoiding discontinuous operation for low current set-points. The DC-DC converter can be seen as formed by two subsystems that can operate as buck or boost converters, which can be synthetically described by the following unified model

7

$$\begin{cases} \dot{I}_L = -\dfrac{V_B}{L_B} + \left(\dfrac{V_{DC}}{L_B}\right) S_w, & \text{(2a)} \\[3mm] \dot{V}_B = g(I_L, \theta), & \text{(2b)} \\[3mm] \dot{V}_{DC} = \dfrac{1}{C_{DC}} \left(I_{DC} - I_{L_{DC}}\right), & \text{(2c)} \end{cases}$$

with $I_{L_{DC}} = I_L S_w$, where I_L is the inductor current, and S_w is the switch state, with $S_w = S_{w1} = \overline{S_{w2}}$, with the over-line denoting the logic inverse state (*i.e.* $S_w = 1$ represents switch closed and $\overline{S_w} = 0$ switch open). The function $g(\cdot)$ is the voltage dynamics of the battery in the linear region, and can be expressed as Buller et al. (2005)

$$g(I_L, \theta) = \frac{1}{Q_B} I_L + R_{int} \dot{I}_L + \epsilon(I_L, \theta), \tag{3}$$

with θ the temperature of the battery, $\epsilon(I_L, \theta)$ a function of the parasite capacitance and other non-linearities, R_{int} the internal resistance of the battery, and Q_B is the capacity of the battery. Since $I_L/Q_B + R_{int}\dot{I}_L \gg \epsilon(I_L)$ for the operating range of the battery voltage, $g(I_L, \theta)$ can be approximated by

$$g(I_L, \theta) \approx \frac{I_L}{Q_B} + R_{int}\dot{I}_L = \frac{I_L}{Q_B} + \frac{R_{int}}{L_B}(V_{DC}S_w - V_B). \tag{4}$$

3. Control of the ESS

The energy stored in the ESS is governed by the controllers K_{GSC} and K_{ESSC} according to the demanded active power P^* and reactive power Q^*. To track the power references, K_{GSC} injects or demands DC current from the DC-link. The DC-link voltage is regulated by the controller K_{ESSC}, which is formed by a linear voltage regulator producing the current set-point for

the faster SM current regulator. This scheme allows the explicit limitation of the current reference to avoid over-current in the power electronic devices and in the battery. The DC-link permits to decouple the design of K_{GSC} and K_{ESSC}; the design of K_{GSC} assumes a constant voltage in the DC-link of the back-to-back converter.

3.1. Grid side converter: power control

The GSC exchanges active and reactive power with the microgrid, according to the power set-points given by a higher level control. For the design of the GSC control, K_{GSC}, it is assumed that the DC-link voltage is constant. The AC power control is typically implemented by regulating the AC current. This current regulator is designed using a PI structure in a rotating DQ frame, a controller widely used with this inverter topology (see *e.g.* Rocabert et al. (2012)). The current controller is

$$\frac{d}{dt} \begin{bmatrix} x_{d_c} \\ x_{q_c} \end{bmatrix} = \begin{bmatrix} k_{i_c} & 0 \\ 0 & k_{i_c} \end{bmatrix} \begin{bmatrix} e_{d_c} \\ e_{q_c} \end{bmatrix},$$

$$\begin{bmatrix} v_{d_o} \\ v_{q_o} \end{bmatrix} = \begin{bmatrix} 1 & 0 \\ 0 & 1 \end{bmatrix} \begin{bmatrix} x_{d_c} \\ x_{q_c} \end{bmatrix} + \begin{bmatrix} k_{p_c} & 0 \\ 0 & k_{p_c} \end{bmatrix} \begin{bmatrix} i_d^* \\ i_q^* \end{bmatrix}$$

$$+ \begin{bmatrix} -k_{p_c} & L_f\omega_n \\ L_f\omega_n & -k_{p_c} \end{bmatrix} \begin{bmatrix} i_d \\ i_q \end{bmatrix} + \begin{bmatrix} 1 & 0 \\ 0 & 1 \end{bmatrix} \begin{bmatrix} v_d \\ v_q \end{bmatrix}, \tag{5}$$

where e_{d_c,q_c} is the difference between the current set-point $i_{d,q}^*$ and the actual current $i_{d,q}$; x_{d_c,q_c} are the states of the controller, $v_{d,q}$ are the grid voltages in DQ frame and v_{d_o,q_o} are the converter voltages generated by the space vector modulation module. The controller parameters K_{I_c}, K_{P_c} are selected

as Harnefors and Nee (1998)

$$K_{P_c} = \frac{L_f}{\tau_c}, \qquad\qquad K_{I_c} = \frac{R_f}{\tau_c}, \qquad\qquad (6)$$

where τ_c is the time constant of the inner current loop. The current references in DQ are computed as

$$\begin{bmatrix} i_d^* \\ i_q^* \end{bmatrix} = \begin{bmatrix} \frac{2}{3v_d} & 0 \\ 0 & \frac{2}{3v_d} \end{bmatrix} \begin{bmatrix} P^* \\ Q^* \end{bmatrix} \qquad\qquad (7)$$

assuming v_q is zero, *i.e.* the the phase-locked loop (PLL) is synchronized with the grid voltage. The resulting closed loop system can be approximated by

$$\frac{d}{dt} \begin{bmatrix} i_{d_c} \\ i_{q_c} \end{bmatrix} = \begin{bmatrix} \frac{-1}{\tau_c} & 0 \\ 0 & \frac{-1}{\tau_c} \end{bmatrix} \begin{bmatrix} i_{d_c} \\ i_{q_c} \end{bmatrix} + \begin{bmatrix} \frac{2}{\tau_c 3v_d} & 0 \\ 0 & \frac{2}{\tau_c 3v_d} \end{bmatrix} \begin{bmatrix} P^* \\ Q^* \end{bmatrix}, \qquad\qquad (8)$$

$$I_{DC} = \frac{P_{grid}}{V_{DC}} = \frac{3v_d i_{d_c}}{2V_{DC}}, \qquad\qquad (9)$$

where I_{DC} (see Fig. 9) is the current drawn from the DC-link by the GSC, and P_{grid} is the actual power exchanged with the microgrid.

3.2. Storage side converter

The objectives of K_{ESSC} are to regulate the DC-link voltage to V_{DC}^*, minimizing voltage excursions in front of the current disturbances produced by K_{GSC}, and to regulate the inductor current I_L. The current I_L must be precisely regulated to avoid over-currents on the sensitive power electronic switches. To fulfill these requirements, a cascaded control scheme is used, as shown in Fig. 1, consisting in a linear voltage regulator and a SM current control. Moreover, K_{ESSC} must provide a very fast transient response in its operation as a voltage regulator, as islanded operation of the microgrid demands fast dynamic responses in front of load or generation changes.

3.2.1. Current control with SM

The DC-DC converter shown in Fig. 2 is clearly a variable structures system, *i.e.*, a system with dynamic changes depending on the conduction state of the switches. It is well known that SM techniques provide quite effective control strategies in the case of variable structures systems Utkin et al. (2009). SM has been chosen instead of linear techniques for the control of the battery current for its performance, robustness and ease of implementation. The DC-DC converter controlled using SM technique provide very fast response without neither overshoot nor risk of modulator saturation but at the expense of a variable switching frequency.

The current regulation can be achieved with a single, simple and easy to implement sliding surface whose reference is modified in correspondence with the voltage controller and the BMS. The power demand can be positive or negative depending on the microgrid operating conditions. Therefore, the DC-DC converter must work in buck mode and boost mode to allow a bidirectional power transfer. To cover all operating modes, the following sliding surface

$$\mathcal{S}(I_L) = I^* - I_L = 0 \tag{10}$$

is proposed associated with the switching logic

$$S_w = (\text{sign}(I^* - I_L) + 1)/2, \tag{11}$$

where sign denotes the sign function and the reference I^* is the set-point given by the voltage regulator. It must be noted that the control law (11) results in infinite variable frequency operation of the power switches. To limit the switching frequency, the current I_L is confined in the region

11

$\{I_L \mid I^* - \Delta I_L < I_L < I^* + \Delta I_L\}$ where ΔI_L is the desired ripple band. The resulting switching frequency depends on the DC voltage levels at both ends of inductance L_B and on the inductance itself, and can be expressed as

$$f_{sw} = \frac{V_{DC}V_B - V_B^2}{2L_B\Delta I_L V_{DC}}, \tag{12}$$

where f_{sw} is the switching frequency. Expression (12) is deduced from Fig. 2 and

$$2\Delta I_L = \frac{\Delta V_L^{sw}}{L_B}\Delta t^{sw}, \tag{13}$$

where ΔV_L^{sw} is the voltage difference across the output inductance, which depends on the switch state, and Δt^{sw} is the time required to produce a variation of $2\Delta I_L$ on the output current.

The sliding surface (10) satisfies the necessary and sufficient condition for sliding mode establishment, a.k.a. transversality condition

$$\mathcal{L}_g\mathcal{S} = -V_{DC}/L_B < 0,$$

where $\mathcal{L}$ is the Lie derivative Utkin et al. (2009). To see this point, the equivalent control is obtained from the invariance condition ($\mathcal{S} = 0$ and $\dot{\mathcal{S}} = 0$) and in the case of the switching law (11) it results

$$S_{w_{eq}} = \frac{V_B}{V_{DC}}. \tag{14}$$

SM regimen exists on the manifold whenever the equivalent control satisfies that $0 \leq S_{w_{eq}} \leq 1$. According to (14), this implies that

$$0 \leq V_B \leq V_{DC}, \tag{15}$$

which is guaranteed by the voltage regulator of the DC-link. The dynamics during SM regimen are obtained by substituting (14) in (2) and is given by

$$
\begin{cases}
\dot{I}_L = 0, & \text{(16a)} \\[2mm]
\dot{V}_B = I^*/Q_B, & \text{(16b)} \\[2mm]
\dot{V}_{DC} = \dfrac{1}{C_{DC}}(I_{DC} - I_{L_{DC}}). & \text{(16c)}
\end{cases}
$$

The stability of the SM controlled system (16) is guaranteed for all initial conditions provided condition (15) is satisfied. Despite $\dot{V}_B$ is not bounded by the SM control, it is indirectly bounded by the BMS. The dynamics of the battery voltage, $\dot{V}_B$, is illustrated in Fig. 4, for three different constant charge currents: $I_{L_1} < I_{L_2} < I_{L_3}$, respecting the BMS limits. As can be seen, $\dot{V}_B$ converges to zero as the voltage reaches the MCV limit. Further details on the prove of stability can be found in Inthamoussou et al. (2013).

3.2.2. Voltage regulation of the DC-link

The DC-link voltage is regulated with a PI control structure with anti-windup compensation, the block K_{DC} in Fig. 5. The output of K_{DC} is the current set-point I^* for the sliding surface (10). For design purposes, the current loop can be assumed in SM regime. Therefore, $I_L = I^*$ and the dynamics of the system to be controlled is given by (16c), denoted as G in Fig. 5

The voltage regulator K_{DC} must reject the current disturbances I_{DC} generated by the GSC, as described in (9), and produce a current set-point $\tilde{I}^*$ for the SM control. This current reference $\tilde{I}^*$ is bounded by the battery lower and higher limits, MDC and MCC respectively, and the current limits of the power electronic switches $\underline{I}$ and $\overline{I}$, *i.e.*

13

$$\max(\underline{I}, MDC) \leq I^* \leq \min(\overline{I}, MCC).$$

The PI controller K_{DC} is governed then by

$$\dot{x}_{K_{DC}} = K_{I_{DC}} e_{DC}, \tag{17}$$

$$\tilde{I}^* = x_{K_{DC}} + K_{P_{DC}} e_{DC}, \tag{18}$$

where $e_{DC} = V_{DC}^* - V_{DC}$, V_{DC}^* is the DC voltage reference, $x_{K_{DC}}$ is the integrator state and $K_{I_{DC}}$ and $K_{P_{DC}}$ are the integral and proportional gains.

Power converters applying standard PWM switching schemes are prone to produce electromagnetic radiation because of the hard switching of the power switches Zhu et al. (2001). This electromagnetic radiation can interfere in the voltage sensors, introducing high frequency noise. As a consequence, it is advisable to limit the controller bandwidth. PI controllers may amplify the high frequency noise. To avoid this undesirable effect, the controller bandwidth is limited by inserting a low-pass filter F into the control loop and by tuning the controller gains using loopshaping ideas.

Let be

$$L(s) = F(s)K_{DC}(s)G(s),$$

$$S(s) = \frac{1}{1 + L(s)}, \qquad\qquad T(s) = \frac{L(s)}{1 + L(s)},$$

the open loop, sensitivity and complementary sensitivity transfer functions, respectively. The sensitivity S is the transfer function from V_{DC}^* to e_{DC} and the complementary sensitivity T is the transfer function from the measurement noise n to V_{DC} (see Fig. 5). In order to achieve a satisfactory voltage regulation, the magnitude of S should be below 0 dB in low frequencies. On

the other hand, the magnitude of T should be below 0 dB in the high frequencies to attenuate the effect of the measurement noise on the controlled variable V_{DC}. Since $S + T = 1$, a compromise must be reached to fulfill both objectives.

Loopshaping allows translating the constraints on the closed loop transfers into constraints on the open loop transfer function L. The constraint on S implies that the magnitude of L must be large in low frequencies, whereas the constraint on T demands small gain in high frequencies. These constraints on the magnitude of L are illustrated in Fig. 6. The magnitude of the open loop transfer function must remain outside the shadows areas. The design based on loopshaping consists in shaping the magnitude of L by selecting proper controller to fulfill the frequency constraints.

Assuming that the close loop bandwidth ω_{DC} is much lower and than the switching frequency $\omega_{sw} = 2\pi f_{sw}$, the dynamics (16c) can be expressed by an average model. Energy balance between battery and DC-link implies

$$\overline{I}_{L_{DC}} V_{DC} = \overline{I}_L V_B, \tag{19}$$

where overline denotes the average value. Thus, (16c) can be expressed in terms of I^* resulting in

$$G(s) = \frac{1}{sC_{DC}} \frac{V_{DC}}{V_B},$$
$$K(s) = k_{P_{DC}} + \frac{k_{I_{DC}}}{s}$$

and assuming the cutoff frequency of filter F, ω_c, is much higher than the closed loop bandwidth ω_{DC}. Since the model of the DC-link depends mainly on the battery voltage V_B (assuming V_{DC} is tightly regulated), the design

15

of the controller parameters can be based on a worst case scenario, this is taking $V_B = \text{MDV}$. This assumption permits to keep the control structure simple and easy to implement. Then the parameters $k_{P_{DC}}$ and $k_{I_{DC}}$ must be chosen in order that the magnitude of

$$L(s) = \frac{k_{P_{DC}}}{C_{DC}} \left(\frac{s + k_{I_{DC}}/k_{P_{DC}}}{s^2} \right) \frac{V_{DC}^*}{\text{MDV}}$$

remains in the non-shadow area in Fig. 6. It is advisable that L crosses the 0 dB line with a slope of -20 dB/decade in order to obtain a damped transient response. Therefore, $k_{I_{DC}}/k_{P_{DC}} \ll \omega_{DC}$ and the gain $k_{P_{DC}}$ is chosen such that the magnitude of L crosses the 0 dB line at ω_{DC}. The bandwidth ω_{DC} should be much lower than filter cutoff frequency ω_c.

Anti-windup scheme

Since, the control variable $\tilde{I}^*$ is limited to protect the battery and the electronic switches, large voltage oversteps could occur as a result of PI windup. Therefore, the voltage controller is completed with a simple anti-windup compensation by back-calculation. As proposed in Åström and Hägglund (1995), the back-calculation coefficient is chosen as $K_B = K_{I_{DC}}$.

4. Experimental Results at full ratings

To illustrate the effectiveness of the proposed control law, it has been implemented in the experimental test bench shown in Fig. 7. The test bench consists of a two stage power converter, composed by the ESSC and the GSC, with its associated controllers. The maximum rated direct current of the ESSC is 20 A, with a total rated power of 4 kW. The battery used in the experimental setup is composed by ten *Synerion (SAFT)* 24 V, 2 kWh

16

module rated at 34 A for charging and 160 A for discharging, with a total capacity of 20 kWh and 240 volts SAFT (2011). The GSC is interfaced with the grid with an a auto-transformer (1), and an isolating transformer (2) for safety reasons (see Fig. 7). The isolation transformer provides galvanic isolation between the AC grid and the power converter. The main parameters of the experimental setup are summarized in Table 1.

To evaluate the proper operation of the proposed control law, the ESS is evaluated in three different scenarios: the black-start operation and positive and negative current disturbance rejection during voltage regulation.

4.1. Black-start operation

The black-start operation consists in the pre-charge of the DC-link with the ESS being disconnected from the grid. This procedure allows re-energizing the microgrid in case of a black-out in the power system or in the microgrid itself. The pre-charge procedure is divided in two steps. First, the battery is connected to the DC-link through a pre-charge resistor, rising V_{DC} up to V_B. This state, $V_{DC} = V_B$, is the limit operating condition that guarantees the stability of the SM current control (15). In the second step of the pre-charge, the SM controller is activated along with the DC-link voltage controller, rising and regulating V_{DC} to V_{DC}^*. The step response of the system can be seen in Fig. 8, where signals V_{DC}, I_L and V_B has been acquired simultaneously.

The signal V_{DC} has been acquired using a differential voltage probe attached directly to the DC-link bus bar; the signal I_L has been acquired using a hall effect DC current probe placed in the cable linking the battery positive pole with the power converter output inductance L_B; the signal V_B has been acquired using a differential voltage probe attached directly to the

17

battery's terminals. Positive currents are defined as the currents delivered by the battery. Note that due to internal losses of the power converter, the average current needed for regulating the voltage to V_{DC}^* is about 2 A. As a consequence of the current ripple and the battery internal resistance R_{int}, the battery voltage also presents a small ripple of 2 V, lower than 0.75%.

Voltage regulation with GSC switching

Lets analyze the interaction between the GSC and the ESSC with the spectrum of V_{DC} shown in Fig. 9. The spectrum corresponds to the DC-link voltage being regulated by ESSC and the GSC regulating active and reactive power to zero. It can be detected three sources of electromagnetic perturbations which deforms the voltage waveform: the grid, the ESSC switching and the GSC switching. In two-level voltage source inverters the grid frequency ripple is induced to the DC-link intrinsically when regulating the AC power to a constant value. This implies that a minimum voltage ripple at the grid frequency will always be present in the DC-link. The variable switching frequency of the SM control scheme results in a flatter spectrum, with the peak value at -70 dB, which doesn't produce significant noise. However, the PWM switching implemented in the GSC results in a high power spike at the switching frequency of 12.21 kHz, with a value of -2.93 dB. This frequency component is attenuated by the low pass filter F to avoid its aliasing in the control loop.

4.2. Current disturbance rejection

During normal operation, the battery can inject or draw power from the microgrid, consuming or injecting current from the DC-link. The task of

K_{ESSC} is to regulate the DC-link voltage by rejecting the current disturbances produced by the GSC. In order to evaluate the performance of the proposed control scheme, the GSC is stepped with a power change from 0 to 100% (0 to 4 kW), and from 0 to -100%. The measured battery power is the product of the battery voltage times the current flowing through the inductor L_B; the grid power is obtained from (7).

Injection of 4 kW to the grid

To validate the effectiveness of the ESSC control scheme, a step of 4 kW is applied at $t = 0.1$ s. The post-disturbance evolution of signals a) V_{DC}, b) I_L, c) battery voltage V_B, d) AC current and e) active power can be seen in Fig. 10. In contrast to Fig. 8 where the GSC is no yet operating, in Fig. 10 the GSC is switching at 12.2 kHz. This power converter produces electromagnetic interferences, resulting in a noisier operation, particularly noticeable in I_L. However, the proper design of K_{DC} and the low pass filter F reduces significantly the signal noise level.

The power set-point change is reflected in the DC-link voltage producing a drop the 2.5 % of V_{DC}^*. The PI voltage regulator produces a current reference that rapidly rejects the disturbance from the GSC, which in turn is perfectly tracked by the SM current controller, as can be seen in Fig. 10. The AC current signals shown correspond to the phase-a current (gray line) and i_d (black line). The instantaneous grid power is shown (black line) in Fig. 10. It must be noted that the actual grid power and the battery drawn power different due to the power losses of the power converter.

Consumption of 4 kW from the grid

During the islanded mode of operation, the ESS can be also charged, consuming power from the microgrid. This situation is analyzed in this scenario, where a set-point of -4 kW is send to the GSC at $t = 0.1$ s. The results of this scenario are shown in Fig. 11, which is analogous to Fig. 10, showing signals a) V_{DC}, b) I_L, c) battery voltage V_B, d) AC current and e) Active power. In this scenario, the voltage V_{DC} rises up to 770 V, 2.5 % higher than V_{DC}^*. The rest of the signals I_L, AC current and active power present characteristics similar to the previous scenario.

5. Conclusion

A new control strategy for a bidirectional AC/DC converter to control the power exchange between a battery and a microgrid has been presented. The proposed strategy combines a unique SM surface, which is able to cover all admissible operating conditions ensuring stability and performance, with a linear voltage regulator for the DC-link voltage. The combination of these two techniques results a in more robust and simpler controller than previous proposals in the literature. The experimental results show that the proposed control strategy exhibits a suitable performance under typical microgrid scenarios, including black-start operation, power injection and battery charging.

Åström, K. J., Hägglund, T., 1995. PID Controllers: Theory, Design, and Tuning, Second Edition. Research Triangle Park, NC: ISA.

Barklund, E., Pogaku, N., Prodanovic, M., Hernandez-Aramburo, C., Green, T., Sep. 2008. Energy Management in Autonomous Microgrid Using Stability-Constrained Droop Control of Inverters 23 (5), 2346–2352.

Barrado, J. A., Aroudi, A. E., Valderrama-Blavi, H., Calvente, J., Martínez-Salamero, L., 2012. Analysis of a Self-Oscillating Bidirectional DC - DC Converter in Battery Energy Storage Applications 27 (3), 1292–1300.

Buller, S., Thele, M., De Doncker, R., Karden, E., 2005. Impedance-based simulation models of supercapacitors and li-ion batteries for power electronic applications 41 (3), 742–747.

Caricchi, F., Crescimbini, F., Giulii Capponi, F., Solero, L., 1998. Study of bi-directional buck-boost converter topologies for application in electrical vehicle motor drives. In: Proc. of Applied Power Electronics Conference and Exposition, APEC. pp. 287 – 293 vol.1.

Delghavi, M. B., Yazdani, A., Apr. 2012. A Unified Control Strategy for Electronically Interfaced Distributed Energy Resources 27 (2), 803–812.

Diaz-Gonzalez, F., Bianchi, F., Sumper, A., Gomis-Bellmunt, O., March 2014. Control of a flywheel energy storage system for power smoothing in wind power plants 29 (1), 204–214.

Erb, D. C., Onar, O. C., Khaligh, A., Feb. 2010. Bi-directional charging topologies for plug-in hybrid electric vehicles. In: Proc. of Applied Power Electronics Conference and Exposition (APEC). IEEE, pp. 2066–2072.

Falahi, M., Lotfifard, S., Ehsani, M., Butler-Purry, K., Oct 2013. Dynamic model predictive-based energy management of dg integrated distribution systems 28 (4), 2217–2227.

Guerrero, J. M., Loh, P. C., Lee, T.-l., Chandorkar, M., 2013. Advanced Control Architectures for Intelligent MicrogridsPart II: Power Quality, Energy Storage, and AC/DC Microgrids 60 (4), 1263–1270.

Harnefors, L., Nee, H.-P., Jan 1998. Model-based current control of ac machines using the internal model control method 34 (1), 133–141.

Inthamoussou, F. A., Pegueroles-Queralt, J., Bianchi, F. D., 2013. Control of a Supercapacitor Energy Storage System for Microgrid Applications 28 (3), 690–697.

Kuperman, A., Levy, U., Goren, J., Zafransky, A., Savernin, A., 2013. Battery Charger for Electric Vehicle Traction Battery Switch Station 60 (12), 5391–5399.

Lasseter, R. H., 2007. Microgrids and Distributed Generation. Journal of Energy Engineering 133 (3), 144.

Levron, Y., Guerrero, J., Beck, Y., 2013. Optimal power flow in microgrids with energy storage 28 (3), 3226–3234.

Marra, F., Yang, G., Traeholt, C., Ostergaard, J., Larsen, E., 2013. A decentralized storage strategy for residential feeders with photovoltaics. IEEE Trans. on Smart Grid PP (99), 1–8.

Oggier, G., Garcia, G., Oliva, A., April 2011. Modulation strategy to operate the dual active bridge dc-dc converter under soft switching in the whole operating range 26 (4), 1228–1236.

Park, G., Gajic, Z., March 2014. A simple sliding mode controller of a fifth-order nonlinear PEM fuel cell model 29 (1), 65–71.

Peças Lopes, J., Moreira, C., Madureira, A., May 2006. Defining Control Strategies for MicroGrids Islanded Operation 21 (2), 916–924.

Qian, H., Zhang, J., Yu, W., 2011. A High-Efficiency Grid-Tie Battery Energy Storage System 26 (3), 886–896.

Rocabert, J., Luna, A., Blaabjerg, F., Rodríguez, P., Nov. 2012. Control of Power Converters in AC Microgrids 27 (11), 4734–4749.

Sable, D. M., Lee, F. C., Cho, B. O. H., 1992. A Zero-Voltage-Switching Bidirectional Battery Charger / Discharger for the NASA EOS Satellite. In: Proc. of Applied Power Electronics Conference and Exposition, APEC. pp. 614–621.

SAFT, march 2011. SYNERION 24 M, medium power lithium-ion module. URL http://www.saftbatteries.com/

Satpathy, A., Kishore, N., Kastha, D., Sahoo, N., 2014. Control scheme for a stand-alone wind energy conversion system PP (99), 1–8.

Tan, S.-C., Lai, Y., Tse, C., 2008. General design issues of sliding-mode controllers in dc-dc converters 55 (3), 1160–1174.

Utkin, V., Guldner, J., Shi, J., 2009. Sliding Mode Control in Electro-Mechanical Systems, Second Edition. CRC Press.

Valverde, L., Rosa, F., Bordons, C., 2013. Design, planning and management of a hydrogen-based microgrid 9 (3), 1398–1404.

Zhu, H., Lai, J.-S., Hefner, A. R., Tang, Y., Chen, C., Sep 2001. Modeling-based examination of conducted emi emissions from hard and soft-switching pwm inverters 37 (5), 1383–1393.

Table 1: Main parameters of the experimental system

Parameter	Value	Units	Description
V_{DC}^*	750	V	Nominal DC-link voltage
V_B	$[210, 280]$	V	Nominal battery voltage range
C_{DC}	2.024	mF	Capacity of the DC-link bus
L_B	4.29	mH	Inductance of the battery branch
$f_{sw_{GSC}}$	12.2	kHz	GSC switching frequency (fixed)
τ_c	10	ms	Power loop response time
$f_{sw_{ESSC}}$	[7-10]	kHz	ESSC switching frequency (variable)
ω_c	250	Hz	low pass filter cut-off frequency
ω_{DC}	100	rad/s	K_{DC} bandwidth
$k_{P_{DC}}$	0.364	-	K_{DC} proportional gain
$k_{I_{DC}}$	22.491	-	K_{DC} integral gain
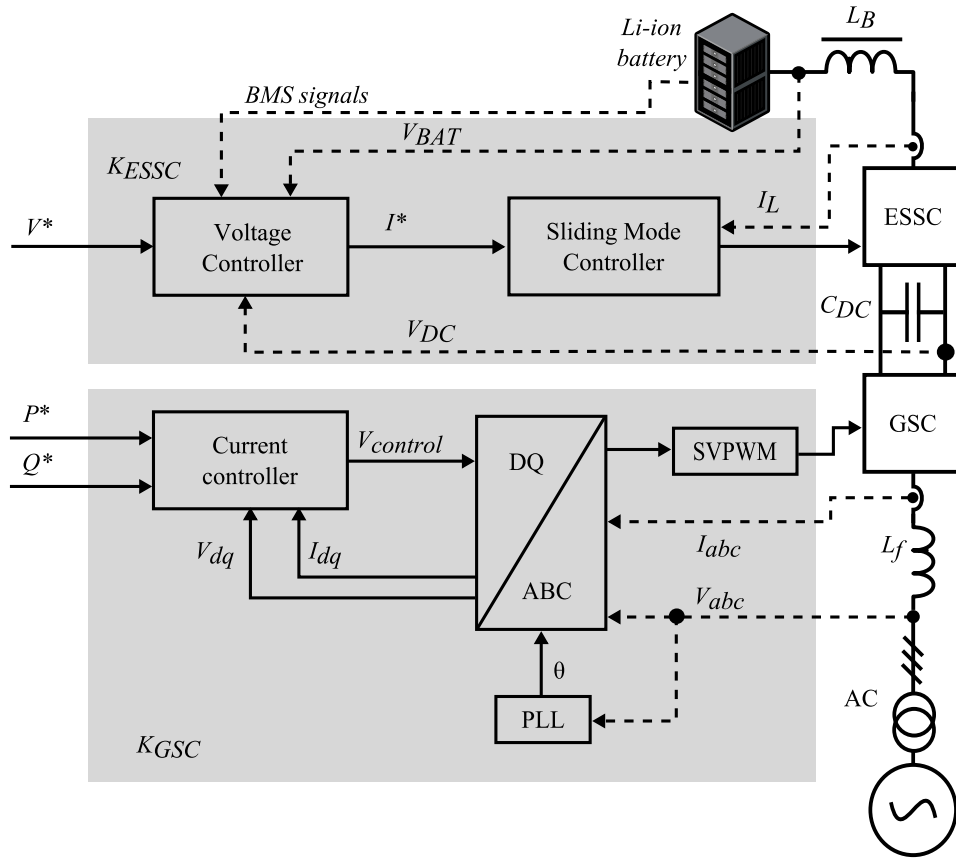
Figure 1: Adopted interface topology for ESS and the power grid
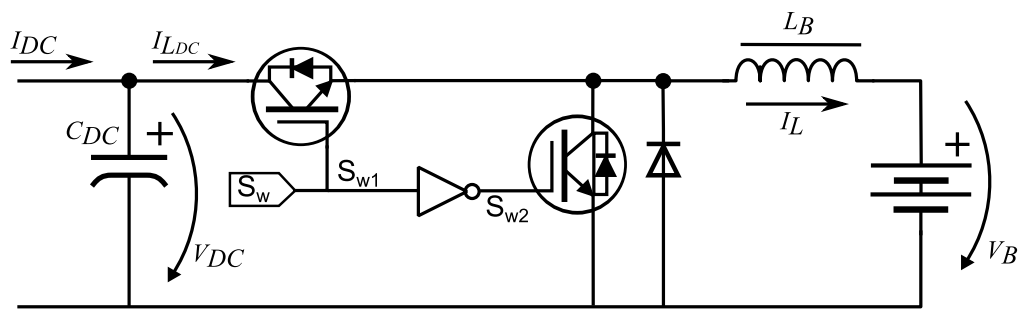
Figure 2: Bidirectional DC-DC topology used in the ESSC
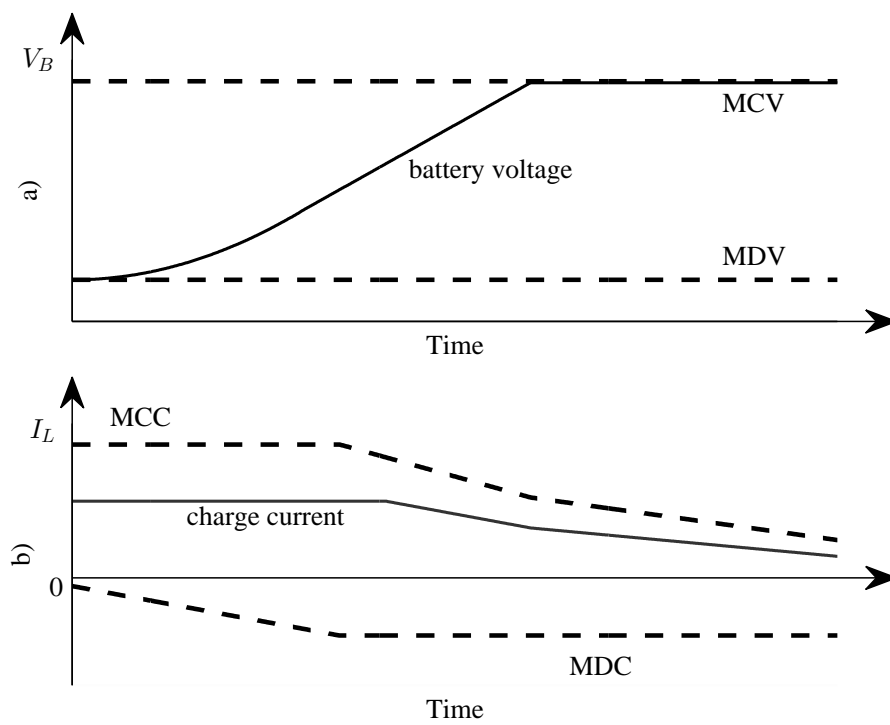
Figure 3: Typical charge profile for medium power lithium-ion batteries
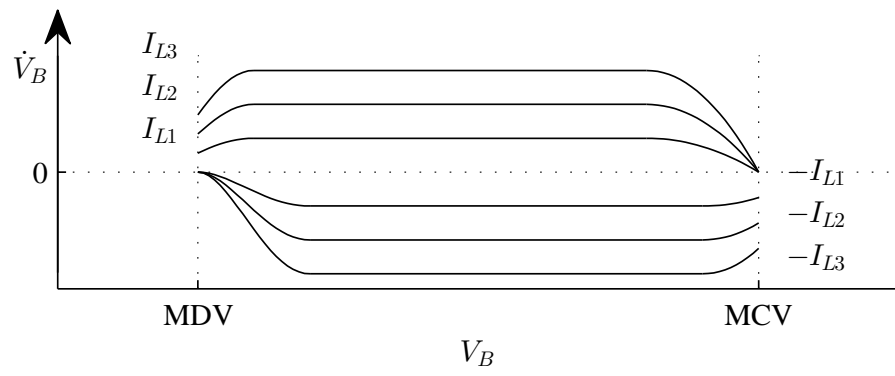
Figure 4: Battery dynamics for three different constant current charge
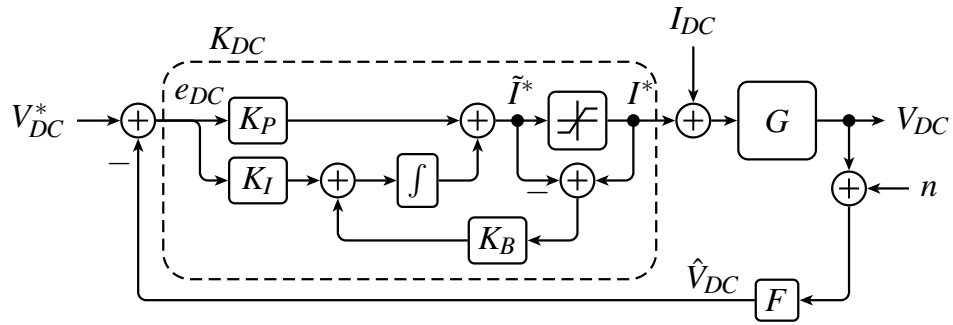
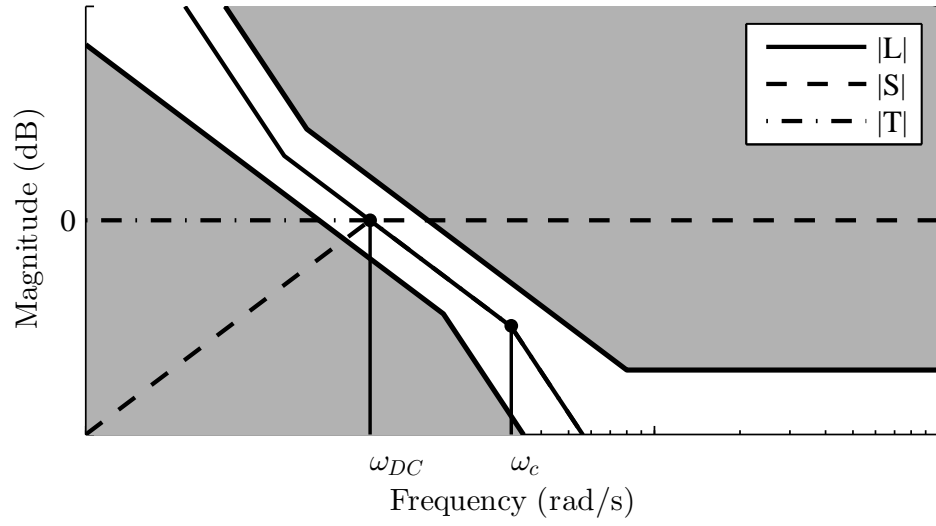Figure 5: Control scheme for the voltage regulation

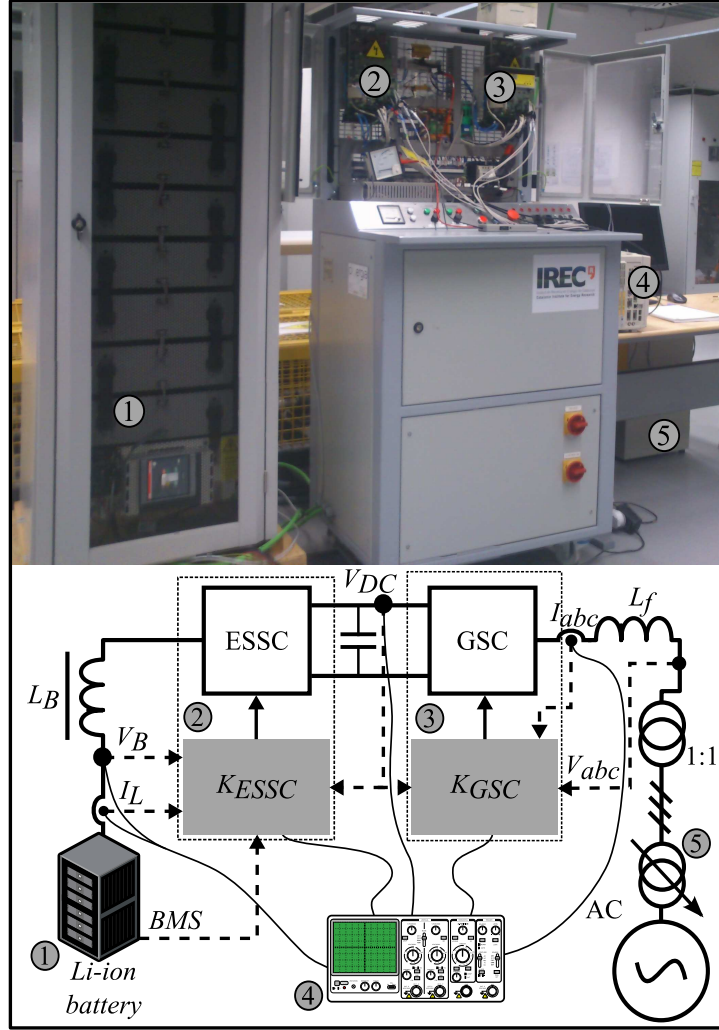Figure 6: Magnitude of L, S, T and the magnitude constraints (shadow area).

Figure 7: Experimental setup used to evaluate the proposed control law with an illustration of the converters, controllers, passive components and measuring points.
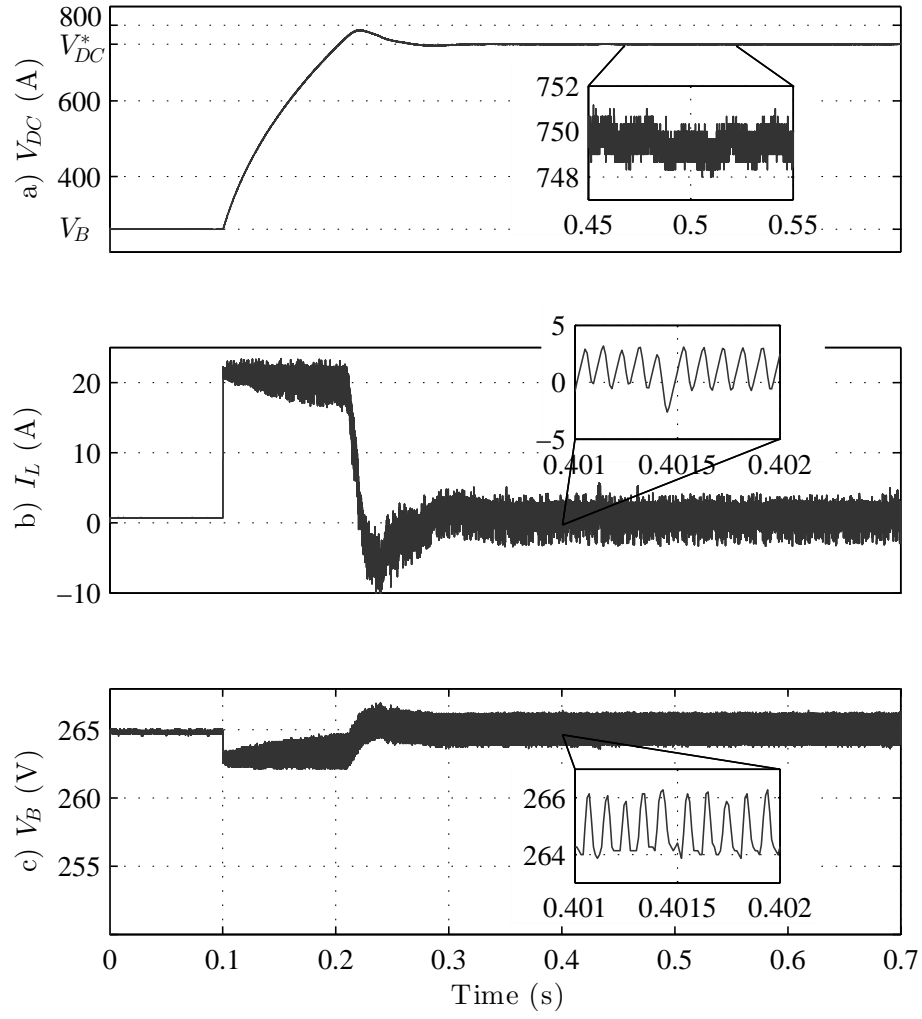
Figure 8: Experimental results during the pre-charge of the DC-link: a) DC-link voltage V_{DC}; b) battery current I_L; c) Battery voltage V_B.
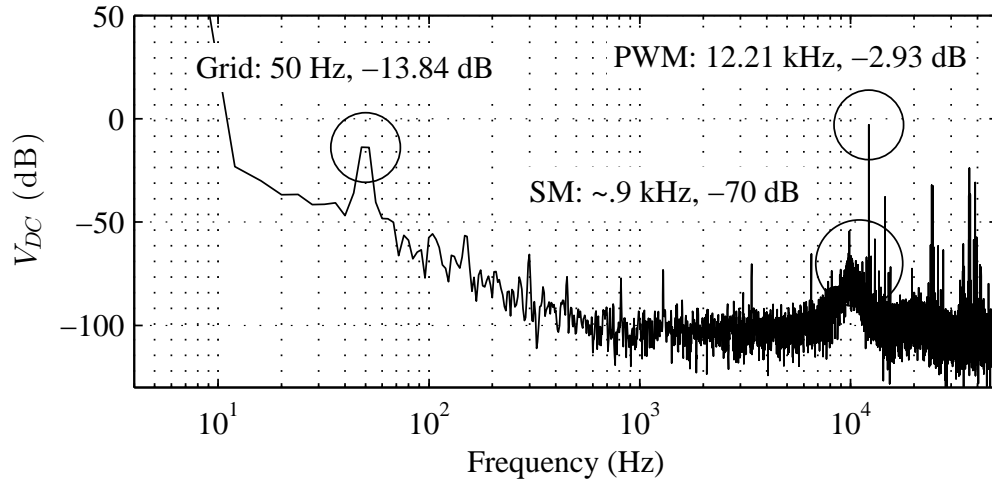
Figure 9: Frequency spectrum of V_{DC}, with the DC-link voltage being regulated by ESSC and the GSC regulating power to zero.
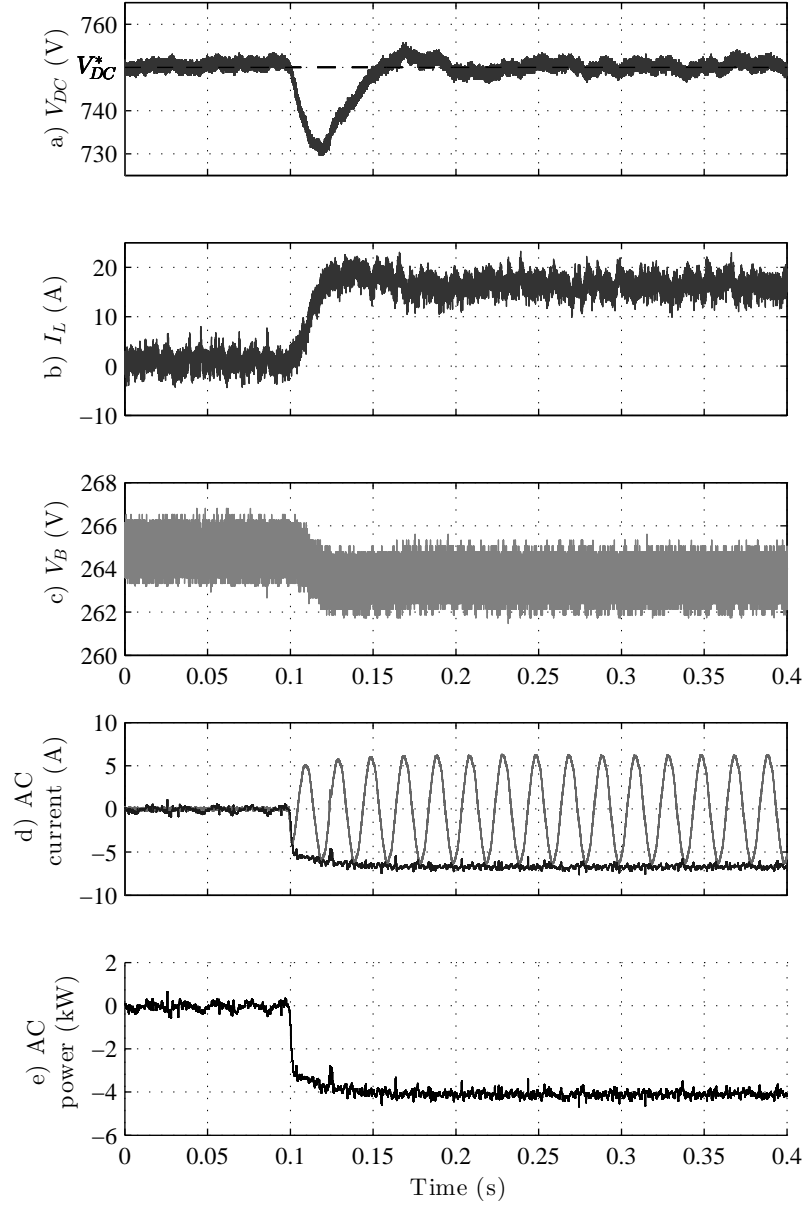
Figure 10: Rejection of a 4 kW power injection disturbance: a) DC-link voltage; b) battery current I_L; c) battery voltage V_B; d) AC current (phase-a, gray; D-axis, black) and e) grid power.
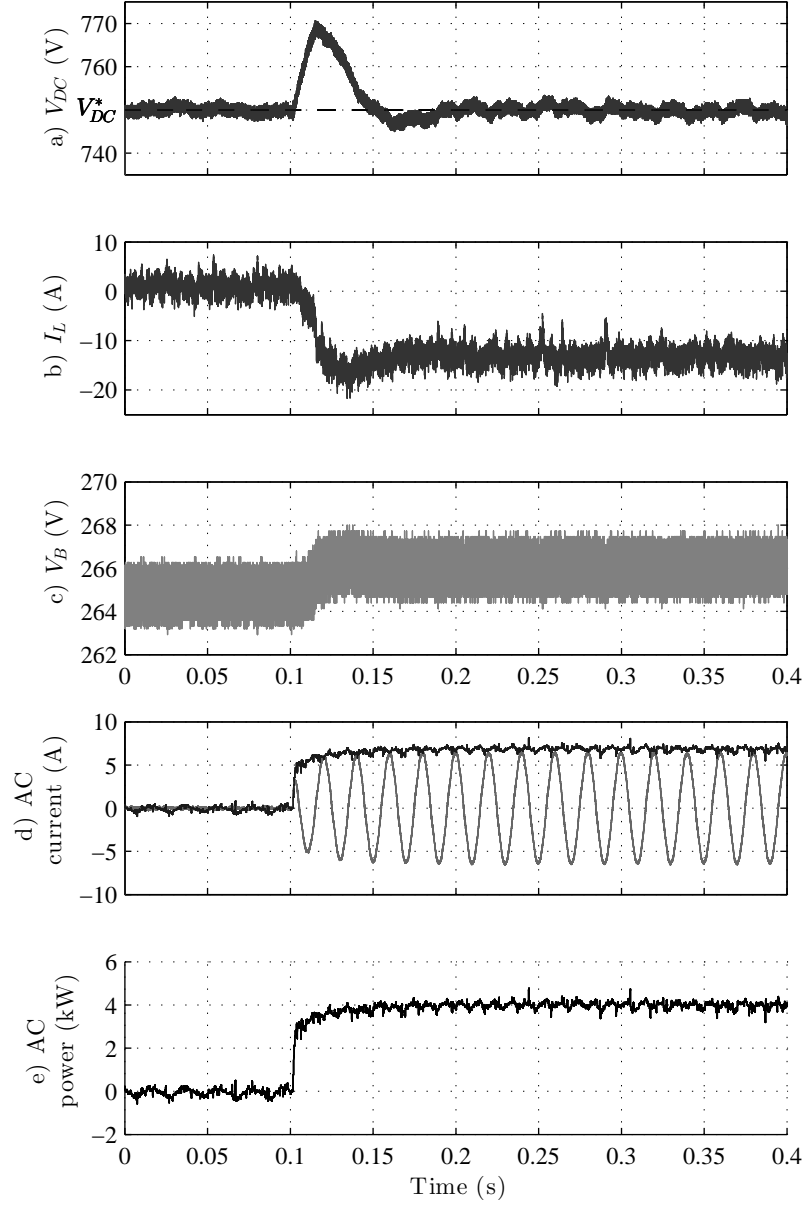
Figure 11: Rejection of a 4 kW power consumption disturbance: a) DC-link voltage; b) battery current I_L; c) battery voltage V_B; d) AC current (phase-a, gray; D-axis, black) and e) grid power.